Supporting Information

Fei et al. 10.1073/pnas.0908077106

SI Methods

Buffer Conditions. Biochemical experiments were performed in Tris-polymix buffer (50 mM Tris-OAc, 100 mM KCl, 5 mM NH_4OAc, 0.5 mM $Ca(OAc)_2$, 10 mM 2-mercaptoethanol, 5 mM putrescine, and 1 mM spermidine) at 15 mM $Mg(OAc)_2$ and at $pH_{25\,°C}$ = 7.5. Single-molecule experiments were conducted in an identical buffer, supplemented with an oxygen-scavenging system (300 μg/mL glucose oxidase, 40 μg/mL catalase and 1% β-D-glucose) (1, 2) and a triplet-state quenching mixture [1 mM 1,3,5,7-cyclooctatetraene (Aldrich) and 1 mM *p*-nitrobenzyl alcohol (Fluka)] (3).

Preparation of Translation Factors, tRNAs, and mRNA. All translation factors were purified as previously reported (1). $tRNA^{fMet}$ was labeled with Cy3-maleimide at the s^4U8 position (1, 4). $tRNA^{fMet}$, (Cy3)$tRNA^{fMet}$, $tRNA^{Phe}$, and $tRNA^{Lys}$ were aminoacylated with the corresponding amino acids, and Met-$tRNA^{fMet}$ and Met-(Cy3)$tRNA^{fMet}$ were formylated, as previously described (1). A T4 gene product 32-derived mRNA was chemically synthesized (Dharmacon) to contain a 5′-biotin followed by an 18 nucleotide spacer, a strong Shine–Dalgarno (AAAGGA) sequence, nucleotides encoding fMet, Phe, Lys, as the first three amino acids, and an additional six amino acids.

***E. coli* L1/L9 Double-Deletion Strain.** L1 and L9 single-deletion strains of *E. coli* were generated from a wild-type *E. coli* strain by using the one-step technique reported by Datsenko and Wanner (5, 6). The original L1 and L9 genes in the wild-type *E. coli* strain were replaced by kanamycin and chloramphenicol resistance cassettes, respectively. The L1/L9 double-deletion strain was subsequently generated by using P1*vir* phage transduction from the single-deletion strains following a protocol provided by Robert T. Sauer (Massachusetts Institute of Technology, Cambridge, MA) (http://openwetware.org/wiki/Sauer:P1vir_phage_transduction) (7). First the L9 single deletion strain was infected with P1*vir* phage. The resulting P1*vir* phage lysate, containing transducing particles carrying random sections of the L9 single-deletion strain genome, including the chloramphenicol resistance cassette located at the former position of the gene encoding L9, was then used to infect a liquid culture of the L1 single-deletion strain. The P1*vir* phage-infected culture of the L1 single deletion strain was plated and colonies exhibiting both kanamycin and chloramphenicol resistance were selected. Deletion of both the L1 and L9 genes was verified by PCR amplification and DNA sequencing. L1 and L9 double-deletion strains exhibit a slow-growth phenotype, with a doubling rate that is ≈6- to 7-fold slower than wild-type *E. coli*.

Purification of 50S Subunits Lacking L1 and L9. The 50S subunits lacking L1 and L9 were purified from the L1/L9 double-deletion strain of *E. coli* by sucrose density gradient ultracentrifugation using a previously described purification protocol (1, 8). Two-dimensional SDS/PAGE was used to verify the absence of L1 and L9 from the purified subunits.

Design and Construction of Fluorescently Labeled L1 and L9 Mutants. The genes encoding *E. coli* L1 and L9 were cloned from C600 genomic DNA into the pProEX-HTb plasmid system, which contains an N-terminal six-histidine (6xHis) affinity purification tag separated from the cloned gene by a tobacco etch virus (TeV) protease cleavage site (1, 8). A Cy5-labeled, single-cysteine (Cys) L1 mutant, L1(T202C), was prepared as previously described, with an ≈65% labeling efficiency (8). An L9 single-Cys mutant, L9(Q18C), was designed by using multiple sequence alignments from a variety of bacterial strains to identify poorly conserved L9 amino acid residues in combination with X-ray crystallographic (9, 10) and cryo-EM structures (11, 12) of ribosomal complexes to identify L9 amino acid residues within FRET distance of our labeling position on L1(T202C). L9(Q18C) was constructed from the pProEX-HTb plasmid bearing the cloned, wild-type L9 gene by using the QuikChange Mutagenesis System (Stratagene) and verified by DNA sequencing. L9(Q18C) was overexpressed and purified by using Ni^{2+}-nitrilotriacetic acid affinity chromatography (Qiagen) under the denaturing buffer conditions specified by the manufacturer. Purified L9(Q18C) was then renatured in renaturation buffer [50 mM sodium phosphate (pH 7.2) and 100 mM NaCl]. The 6xHis tag was subsequently cleaved by incubating L9(Q18C) with TeV protease at 4 °C overnight in renaturation buffer. Cleaved L9(Q18C) was purified from the cleaved 6xHis tag, uncleaved L9(Q18C), and TeV protease by using a second Ni^{2+}-nitrilotriacetic acid affinity chromatography step in renaturation buffer. Fluorescent labeling of L9(Q18C) with Cy3-maleimide (GE Lifesciences) was performed by incubating 40 μM L9(Q18C) and 800 μM Cy3-maleimide at room temperature for 2 h in a buffer containing 50 mM Tris·HCl ($pH_{25\,°C}$ = 7.0), 200 mM KCl, 4 mM Tris(2-carboxyethyl)phosphine (TCEP) and 4 M urea. Cy3-labeled L9(Q18C) was purified from free, unreacted dye by gel filtration on Superdex 75 in a buffer containing 20 mM Tris·HCl ($pH_{4\,°C}$ 7.5), 400 mM NH_4Cl, 4 mM $MgCl_2$ and 4 M urea. Buffers for purifying, labeling, and storing L9(Q18C) contained urea to prevent the aggregation and precipitation of L9(Q18C), which is observed in the absence of its ribosomal binding partner. Based on a comparison of Cy3 and L9(Q18C) concentrations determined from Cy3 absorbance at 550 nm (extinction coefficient = 150,000 M^{-1} cm^{-1}) and an L9(Q18C) Bradford assay, we estimate ≈50% labeling of L9(Q18C).

Preparation of Dual-Labeled 50S Subunits. Cy5-labeled L1(T202C) and Cy3-labeled L9(Q18C) were reconstituted into purified 50S ribosomal subunits lacking L1 and L9 by using previously described protocols (13, 14). Reconstituted, dual-labeled 50S subunits were subjected to sucrose density gradient ultracentrifugation to separate free, unincorporated, Cy5-labeled L1(T202C) and Cy3-labled L9(Q18C) from dual-labeled 50S subunits. Based on spectrophotometrically determined 50S subunit, Cy5, and Cy3 concentrations, we estimate a reconstitution efficiency of ≈100% for Cy5-labeled L1(T202C) and ≈60% for Cy3-labeled L9(Q18C). Given labeling efficiencies of ≈65% and ≈50% for L1(T202C) and L9(Q18C), respectively, dual-labeled 50S subunits are estimated to contain ≈65% Cy5-labeled L1(T202C) and ≈30% Cy3-labeled L9(Q18C). However, only those 50S subunits carrying both Cy5-labeled L1(T202C) and Cy3-labeled L9(Q18C) will generate an observable $smFRET_{L1\text{-}L9}$ signal in our experiments. Ribosomes lacking Cy5-labled L1(T202C) and/or Cy3-labeled L9(Q18C) or harboring unlabeled L1(T202C) and/or L9(Q18C) are not detected and do not affect either the collected $smFRET_{L1\text{-}L9}$ data or its analysis.

Biochemical Characterization of Dual-Labeled 50S Subunits. A standard primer-extension inhibition, or toeprinting, assay (15, 16) was used to test the ability of dual-labeled 50S subunits, 30S subunits, and fMet-$tRNA^{fMet}$ to properly initiate on a defined

mRNA in the presence of initiation factors 1, 2, and 3 and GTP. Toeprinting was also used to verify that these ribosomal initiation complexes could undergo peptide-bond formation and translocation through two rounds of translation elongation. The results shown in Fig. S1 demonstrate that ribosomes harboring dual-labeled 50S subunits can undergo all of these reactions with an efficiency that is indistinguishable from that observed for ribosomes harboring wild-type 50S subunits. Based on these toeprinting results, we estimate that, upon addition of EF-Tu(GTP)Phe-tRNA^{Phe} and EF-G, INI is ≈90% active through the first round of translation elongation necessary to generate POST$_{fM/F}$ and, upon further addition of EF-Tu(GTP)Lys-tRNA^{Lys} and EF-G, POST$_{fM/F}$ is ≈70% active in the second round of translation elongation necessary to generate POST$_{F/K}$.

Purification and Surface Immobilization of Ribosomal Complexes. INI and POST$_{fM/F}$ complexes for smFRET$_{L1\text{-}L9}$ studies were enzymatically prepared on our 5′-biotinylated, T4 gene product 32-derived mRNA by using dual-labeled 50S subunits, 30S subunits, and all necessary initiation and/or elongation factors and aminoacyl-tRNAs. Likewise, ribosomal complexes analogous to INI and POST$_{fM/F}$ complexes but containing Cy5-labeled 50S subunits and Cy3-labeled P-site tRNAs for smFRET$_{L1\text{-}tRNA}$ experiments were enzymatically prepared on the same mRNA by using 50S subunits harboring a Cy5-labled L1 protein, 30S subunits, and all necessary initiation and/or elongation factors and aminoacyl-tRNAs, including either fMet-(Cy3)tRNA^{fMet} or Phe-(Cy3)tRNA^{Phe} (8). The resulting complexes were separated from free mRNA, translation factors, and aminoacyl-tRNAs by sucrose density gradient ultracentrifugation as previously described (1, 8). Purified ribosomal complexes were immobilized via a biotin-streptavidin interaction onto the surface of a streptavidin-derivatized quartz flow cell. As previously reported, before immobilization of ribosomal complexes, quartz flow cells were passivated by amino silanization followed by reaction with a mixture of *N*-hydroxysuccinimide ester-activated polyethyleneglycol (PEG) and PEG-biotin. Passivated flow cells were incubated with streptavidin just before use (1, 8).

Total Internal Reflection Fluorescence Microscopy. We have designed and constructed a home-built, wide-field, prism-based total internal reflection fluorescence microscope using a 532-nm laser (Crysta-Laser) as an excitation source and a 512 × 512 pixel, back-thinned CCD camera (Cascade II; Princeton Instruments) as a detector. This microscope allows direct visualization of ≈200–300 ribosomal complexes in an observation area of 60 × 120 μm^2. All smFRET$_{L1\text{-}L9}$ data were collected under 11mW excitation laser power with 0.10 sec frame^{-1} time resolution; all smFRET$_{L1\text{-}tRNA}$ data were collected under 15 mW excitation laser power with 0.05 sec frame^{-1} time resolution. Single ribosomes were identified by single-step fluorophore photobleaching.

smFRET$_{L1\text{-}L9}$ data were recorded by using a 0.10 sec frame^{-1} time resolution to maximize the signal-to-noise such that transitions between the relatively closely spaced 0.34 and 0.56 FRET states (corresponding to a 0.22 FRET difference) could be easily identified and analyzed. The smFRET$_{L1\text{-}tRNA}$ data were recorded by using a 0.05 sec frame^{-1} time resolution to remain consistent with, and allow direct comparison to, our previously reported smFRET$_{L1\text{-}tRNA}$ data (8) Transitions between the relatively further spaced 0.21 and 0.84 FRET states (corresponding to a 0.63 FRET difference) for the smFRET$_{L1\text{-}tRNA}$ data recorded by using Cy3-labeled tRNA^{Phe} at the P-site (8) or 0.10 and 0.60 FRET states (corresponding to a 0.50 FRET difference) for the smFRET$_{L1\text{-}tRNA}$ data recorded by using Cy3-labeled tRNA^{fMet} at the P-site (the current work) are easily observed regardless of the slightly lower signal-to-noise in the higher-time resolution data.

Selection of smFRET vs. Time Trajectories. Raw fluorescence intensity data were analyzed with the MetaMorph software suite (Molecular Devices). Selection of smFRET trajectories was performed as previously described (8). Because of imperfect performance of emission filters, which allow a small amount of Cy3 emission to bleed through into the Cy5 emission channel, the Cy5 intensity of each trace was corrected by using bleed-through coefficient of 7% (experimentally measured by using Cy3-labeled DNA oligonucleotides). Both Cy3 and Cy5 intensities were baseline corrected such that the averaged postphotobleaching intensity for both fluorophores is centered at zero intensity. FRET values were calculated by using $I_{Cy5}/(I_{Cy3}+I_{Cy5})$, where I_{Cy3} and I_{Cy5} are the emission intensities for Cy3 and Cy5, respectively, for each baseline-corrected pair of Cy3 and Cy5 data points in each trace (8).

Dwell Time Analysis. Each smFRET trajectory was idealized as a hidden Markov model, by using the vbFRET software package (17)—open source MATLAB code to be available at vbfret.sourceforge.net upon acceptance of manuscript for publication). vbFRET infers the idealized trajectory by using a variational Bayesian analysis (rather than maximum likelihood) (18), which also determines kinetic parameters as well as the number of conformational states for individual trajectories, thereby avoiding overfitting. Although rare, transitions in the idealized smFRET trajectories occurring with a change of <0.05 FRET or 0.1 FRET were discarded from the analysis of smFRET$_{L1\text{-}L9}$ or smFRET$_{L1\text{-}tRNA}$ datasets, respectively. For each dataset, the data points from the entire set of idealized smFRET trajectories were used to generate a one-dimensional FRET histogram. Origin7.0 was used to fit each histogram with three Gaussian distributions by using initial guesses centered at 0, 0.35, and 0.55 for smFRET$_{L1\text{-}L9}$ and centered at 0, 0.10 and 0.65 for smFRET$_{L1\text{-}tRNA}$. Thresholds for each FRET state were set by using the full width at half-height of the Gaussian distribution. By using these thresholds, the dwell time in each state before transitioning was extracted from the idealized smFRET trajectories. One-dimensional population vs. time histograms were plotted and lifetimes were determined by fitting the histogram to either a single- or double-exponential decay (Fig. S2). Transition rates were calculated by taking the inverse of the lifetimes and applying corrections for premature truncation due to photobleaching as well as the finite nature of the trajectory. (refs. 19 and 20 and Table S1).

Subpopulation and Dwell Time Analysis of PMN$_{F/-}$ + EF-G(GDPNP). Binding of EF-G(GDPNP) to PMN$_{F/-}$ strongly inhibits closed → open L1 stalk transitions such that the open ⇄ closed L1 stalk equilibrium shifts to favor the closed L1 stalk conformation and the rate of photobleaching from the closed L1 stalk conformation effectively out competes closed → open transitions; the overall effect is a decrease in the occupancy of SP$_{fluct}$ and a corresponding increase in the occupancy of SP$_{closed}$. Because EF-G(GDPNP)-bound PMN$_{F/-}$ occupies SP$_{closed}$, k_{open} and k_{close} for EF-G(GDPNP)-bound PMN$_{F/-}$ cannot be calculated (Table 1). Despite this, Fig. 2*B* reveals that 23% of the PMN$_{F/-}$ + EF-G(GDPNP) trajectories remain in SP$_{fluct}$. Analysis of SP$_{fluct}$ in this scenario is complicated by the compositional heterogeneity present in PMN$_{F/-}$ + EF-G(GDPNP) that arises from incomplete reactivity at each of the various enzymatic steps required to prepare PMN$_{F/-}$ + EF-G(GDPNP) (i.e., reaction of INI with EF-Tu(GTP)Phe-tRNA^{Phe} to generate PRE$_{fM/F}$, reaction of PRE$_{fM/F}$ with EF-G to form POST$_{fM/F}$, puromycin reaction of POST$_{fM/F}$ to form PMN$_{F/-}$, and binding of EF-G(GDPNP) to PMN$_{F/-}$). Of these potential sources of heterogeneity, the ones that primarily contribute to SP$_{fluct}$ in PMN$_{F/-}$ + EF-G(GDPNP) are: (*i*) binding of EF-G(GDPNP) to a residual amount [estimated at ≈10% (Fig. S1)] of PMN$_{fM/-}$ that

arises from puromycin reaction of INI that failed to undergo elongation. This source of heterogeneity can be easily resolved by investigating EF-G(GDPNP)-bound $PMN_{fM/-}$ (Table 1 and Table S2); (*ii*) $PRE_{F/-}$ that failed to bind EF-G(GDPNP). This source of heterogeneity can be resolved by using the dwell time analysis of $PMN_{F/-}$ in the absence of EF-G(GDPNP) (Table 1 and Table S2). All other potential sources of compositional heterogeneity (i.e., $PMN_{fM/-}$ that failed to bind EF-G(GDPNP) or INI or $POST_{fM/F}$ that failed to undergo puromycin reaction) are either negligible or result in trajectories that primarily occupy $SP_{open,}$ thus not affecting the dwell time analysis of SP_{fluct}.

Based on the sources of heterogeneity described above, the dwell time histogram for the open L1 stalk conformation of $PMN_{F/-}$ in the presence of 1 μM EF-G(GDPNP) was fit with a double-exponential decay in which A_1 represents the relative population of transition events contributed by $PMN_{F/-}$ that failed to bind EF-G(GDPNP) and A_2 represents the relative population of transition events contributed by EF-G(GDPNP)-bound $PRE_{fM/-}$. To convert the relative populations of transition events, A_1 and A_2, into relative populations of trajectories, P_1 and P_2, we need to account for the fact that the fast-transitioning population of trajectories, P_2, will have a larger contribution to the total number of transition events than the slow-transitioning trajectory population, P_1. Based on the A_1 and A_2 lifetimes, 1.5 sec and 0.35 sec, respectively, the ratio of "transition frequencies" for P_1 and P_2 can be estimated as 0.35:1.5. Thus, solving the following equation: $(0.35P_1)/(1.5P_2) = A_1/A_2 = 14/86$, yields $P_1/P_2 = 0.7$. Therefore, (23%) $[0.7/(1 + 0.7)] = 9\%$ is the percentage of $PRE_{F/-}$ complexes that do not bind EF-G(GDPNP) and $23\% - 9\% = 14\%$ is the percentage of contaminating $PRE_{fM/-}$ complexes. These results are consistent with our toeprinting activity assays (Fig. S1) and are further supported by dwell time analyses of $PRE_{F/-}$ as a function of EF-G(GDPNP) concentration, in which A_1 decreases and A_2 increases with increasing concentrations of EF-G(GDPNP) (Table S2).

1. Blanchard SC, et al. (2004) tRNA dynamics on the ribosome during translation. *Proc Natl Acad Sci USA* 101:12893–12898.
2. Stone MD, et al. (2007) Stepwise protein-mediated RNA folding directs assembly of telomerase ribonucleoprotein. *Nature* 446:458–461.
3. Gonzalez RL, Jr, Chu S, Puglisi JD (2007) Thiostrepton inhibition of tRNA delivery to the ribosome. *RNA* 13:2091–2097.
4. Watson BS, et al. (1995) Macromolecular arrangement in the aminoacyl-tRNA.elongation factor Tu.GTP ternary complex. A fluorescence energy transfer study. *Biochemistry* 34:7904–7912.
5. Datsenko KA, Wanner BL (2000) One-step inactivation of chromosomal genes in *Escherichia coli* K-12 using PCR products. *Proc Natl Acad Sci USA* 97:6640–6645.
6. Baba T, et al. (2006) Construction of *Escherichia coli* K-12 in-frame, single-gene knockout mutants: The Keio collection. *Mol Syst Biol* 2:2006 0008.
7. Sternberg N, Hoess R (1983) The molecular genetics of bacteriophage P1. *Annu Rev Genet* 17:123–154.
8. Fei J, Kosuri P, MacDougall DD, Gonzalez RL, Jr (2008) Coupling of ribosomal L1 stalk and tRNA dynamics during translation elongation. *Mol Cell* 30:348–359.
9. Schuwirth BS, et al. (2005) Structures of the bacterial ribosome at 3.5 A resolution. *Science* 310:827–834.
10. Nikulin A, et al. (2003) Structure of the L1 protuberance in the ribosome. *Nat Struct Biol* 10:104–108.
11. Valle M, et al. (2003) Locking and unlocking of ribosomal motions. *Cell* 114:123–134.
12. Agirrezabala X, et al. (2008) Visualization of the hybrid state of tRNA binding promoted by spontaneous ratcheting of the ribosome. *Mol Cell* 32:190–197.
13. Odom OW, Picking WD, Hardesty B (1990) Movement of tRNA but not the nascent peptide during peptide bond formation on ribosomes. *Biochemistry* 29:10734–10744.
14. Ermolenko DN, et al. (2007) Observation of intersubunit movement of the ribosome in solution using FRET. *J Mol Biol* 370:530–540.
15. Hartz D, McPheeters DS, Traut R, Gold L (1988) Extension inhibition analysis of translation initiation complexes. *Methods Enzymol* 164:419–425.
16. Fredrick K, Noller HF (2002) Accurate translocation of mRNA by the ribosome requires a peptidyl group or its analog on the tRNA moving into the 30S P site. *Mol Cell* 9:1125–1131.
17. Bronson JE, Fei J, Hofman JM, Gonzalez RL, Jr, Wiggins CH (2009) Learning rates and states from biophysical time series: A Bayesian approach to model selection and single-molecule FRET data. arXiv:0907.3156 [q-bio.QM], http://arxiv.org/pdf/0907.3156.
18. Jordan MI, Ghahramani Z, Jaakkola TS, Saul LK (1999) An introduction to variational methods for graphical models. *Machine Learn* 37:183–233.
19. Bartley LE, et al. (2003) Exploration of the transition state for tertiary structure formation between an RNA helix and a large structured RNA. *J Mol Biol* 328:1011–1026.
20. Sternberg SH, et al. Translation factors direct intrinsic ribosome dynamics during termination and ribosome recycling. *Nat Struct Mol Biol* 16:861–868.

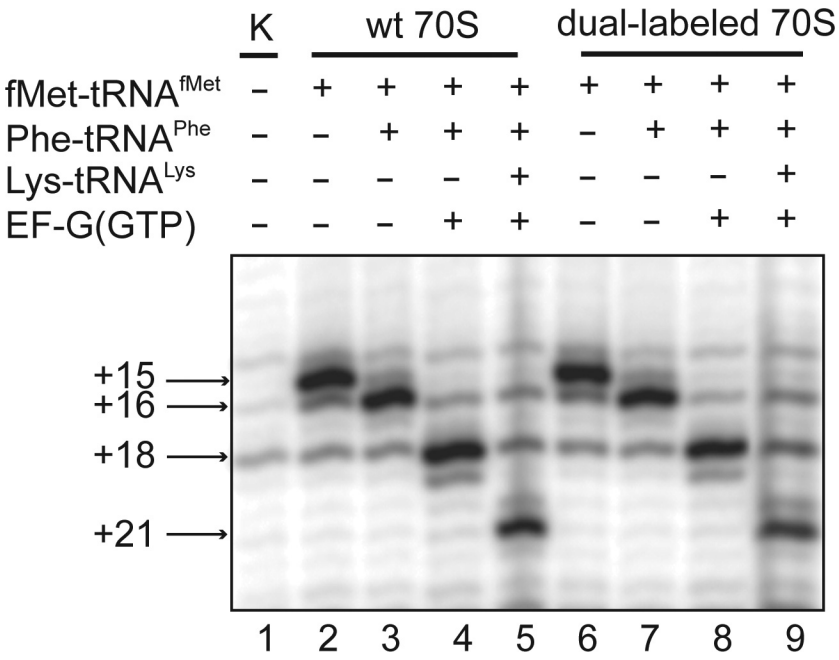

Fig. S1. Primer-extension inhibition, or toeprinting, assay. The activity of ribosomes harboring reconstituted, dual-labeled 50S subunits was tested by using a primer-extension inhibition, or toeprinting, assay (15, 16). Translation reactions were performed by using all purified components and an mRNA preannealed with a ^{32}P-labeled DNA primer. The position of the initiated ribosomal complex on the mRNA was determined by monitoring the inhibition of a subsequent reverse transcription reaction and running the cDNA products of the reverse transcription reaction on a denaturing PAGE. cDNA bands corresponding to mRNA positions +15, +16, +18, and +21, relative to the A of the AUG start codon that comprises position 0, report on the initiated ribosomal complex (+15), the incorporation of the first A-site tRNA (Phe-tRNA^{Phe}) (+16), the first translocation step (+18), and, collectively, the incorporation of a second A-site tRNA (Lys-tRNA^{Lys}) and translocation step (+21). Lane 1 is a control generated by reverse transcription of the ^{32}P-labeled primer-annealed mRNA in the absence of ribosomes; this control reports on intrinsic reverse transcriptase inhibition sites likely caused by regions of stable secondary structures within the mRNA. Raw intensities at mRNA nucleotide positions +15, +16, +18, and/or +21 in lanes 2–9 were therefore corrected by using the lane 1 intensities at the corresponding positions. Comparison of the corrected bands at +15, +18, and +21 in lanes 7–9 suggest that initiated ribosomal complexes are ≈90% active in the first round of elongation and ≈70% active in the second round of elongation. These activities are indistinguishable from those of wild-type ribosomes (lanes 3–5).

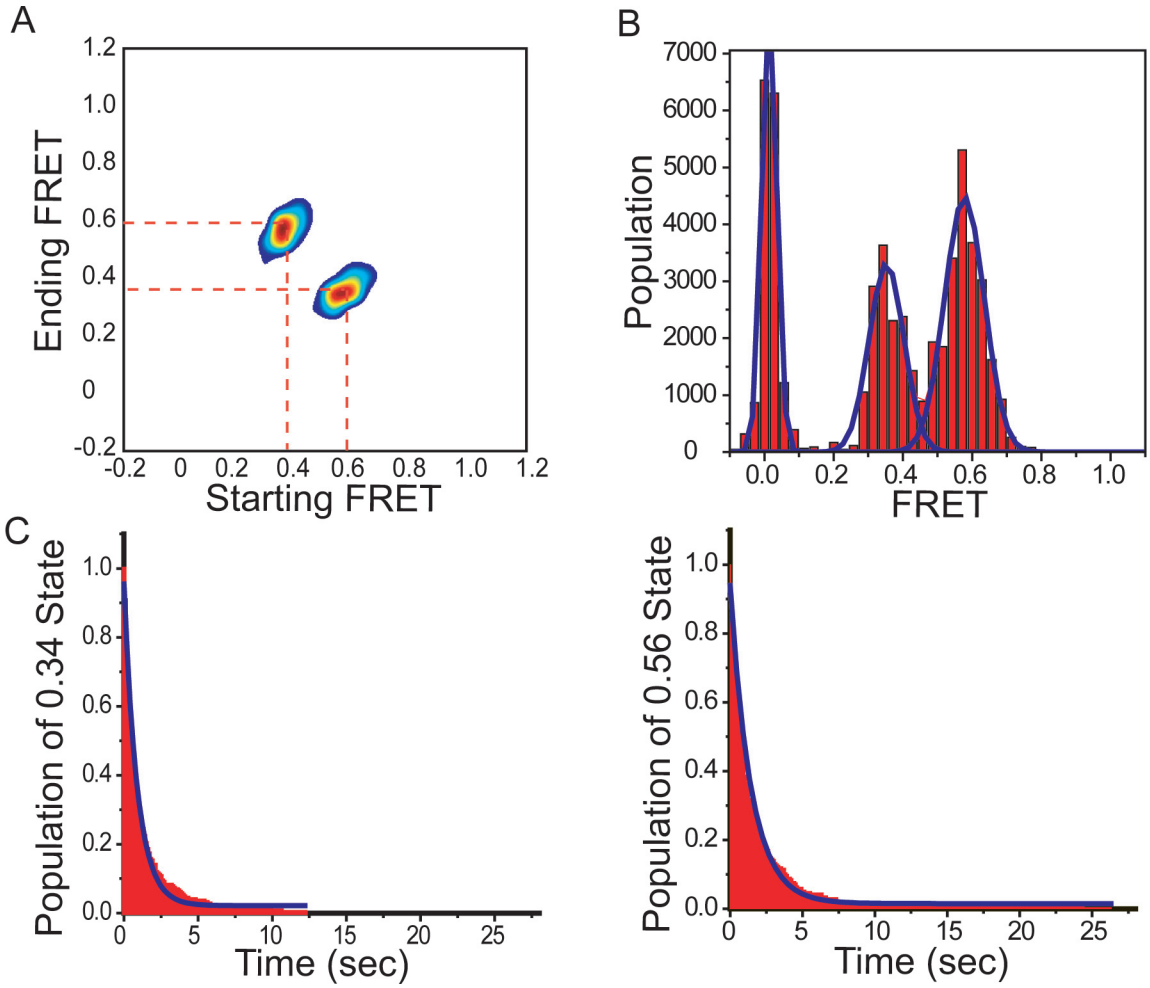

Fig. S2. Sample dwell time analysis. (*A*) A transition density plot for each complex is generated by plotting the ''Starting FRET'' versus the ''Ending FRET'' for each transition as a surface contour plot of two-dimensional population histograms. Contours are plotted from tan (lowest population) to red (highest population). (*B*) One-dimensional FRET histograms calculated from the idealized smFRET trajectories generated by hidden Markov modeling of the raw smFRET trajectories using vbFRET (17, 18) (open source MATLAB code available at vbfret.sourceforge.net). Initial thresholds for each FRET state were determined by fitting these histograms to three Gaussian distributions with user-specified initial guess values of 0, 0.35, and 0.55 FRET for the Gaussian centers and by using the full width at half-height of the resulting Gaussians as initial threshold values. (*C*) Dwell time histograms in the 0.56 FRET and 0.34 FRET states are described either by a single-exponential decay ($A*\exp(-t/t_0) + y_0$) or a double-exponential decay ($A_1*\exp(-t/t_1) + A_2*\exp(-t/t_2) + y_0$).

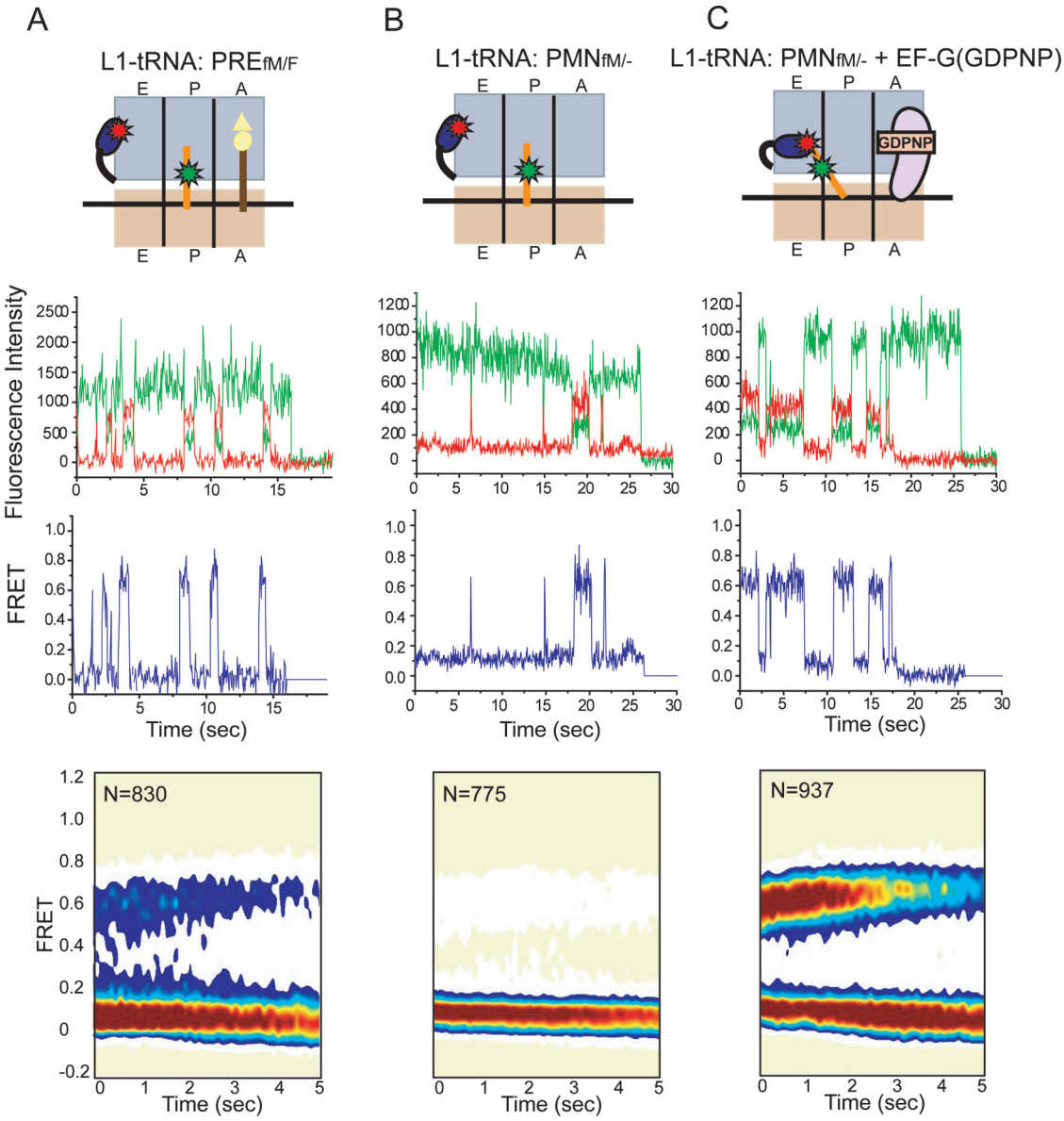

Fig. S3. Steady-state smFRET$_{L1\text{-}tRNA}$ of PRE and PMN complexes analogous to PRE$_{fM/F}$ and PMN$_{fM/-}$ in the absence and presence of 1 μM EF-G(GDPNP). Cartoon representations of PRE and PMN complexes analogous to PRE$_{fM/F}$ and PMN$_{fM/-}$ depict the 30S and 50S subunits in tan and lavender, respectively, with the L1 stalk in dark blue, tRNA^{fMet} as an orange line, EF-G in light purple, and Cy5 and Cy3 as red and green stars, respectively (first row). Representative Cy3 and Cy5 emission intensities are shown in green and red, respectively (second row). The corresponding smFRET vs. time trajectories, in which the FRET efficiency is calculated by using the equation $I_{Cy5}/(I_{Cy3} + I_{Cy5})$, where I_{Cy3} and I_{Cy5} are the emission intensities of Cy3 and Cy5, respectively, are shown in blue (third row). Surface contour plots of the time evolution of population FRET are plotted from tan (lowest population) to red (highest population) (bottom row). The number of traces that were used to construct each contour plot is indicated by ''N.'' (*A*) PRE complex analogous to PRE$_{fM/F}$, generated by addition of 100 nM EF-Tu(GTP)Phe-tRNA^{Phe} to a ribosomal initiation complex analogous to INI. (*B*) PMN complex analogous to PMN$_{fM/-}$, generated by addition of 1 mM puromycin to a ribosomal initiation complex analogous to INI, in the absence of EF-G(GDPNP). (C) PMN complex analogous to PMN$_{fM/-}$ in the presence of 1 μM EF-G(GDPNP). The 0.10 and 0.60 FRET states here correspond to the 0.21 and 0.84 FRET states measured previously (8). The slightly lower FRET values reported in the present work are due to the different labeling position on tRNA^{fMet} (s^4U8, this work) vs. tRNA^{Phe} [acp^{3}U47, previous work (8)] as well as the use of a slightly different image-splitting device for separating the Cy3 and Cy5 emission wavelengths (Dual-View; Photometrics), this work vs. Quad-View (Photometrics), previous work (8). We note here the observation that the smFRET$_{L1\text{-}tRNA}$ signals for PRE$_{fM/F}$ and PMN$_{fM/-}$ exhibit poor signal-to-noise relative to PRE$_{F/K}$ and PMN$_{F/-}$; this is due to the higher noise in the Cy3 donor signal when Cy3 is covalently attached to the s^4U8 position of tRNA^{fMet} vs. the acp^{3}U47 position of tRNA^{Phe}.

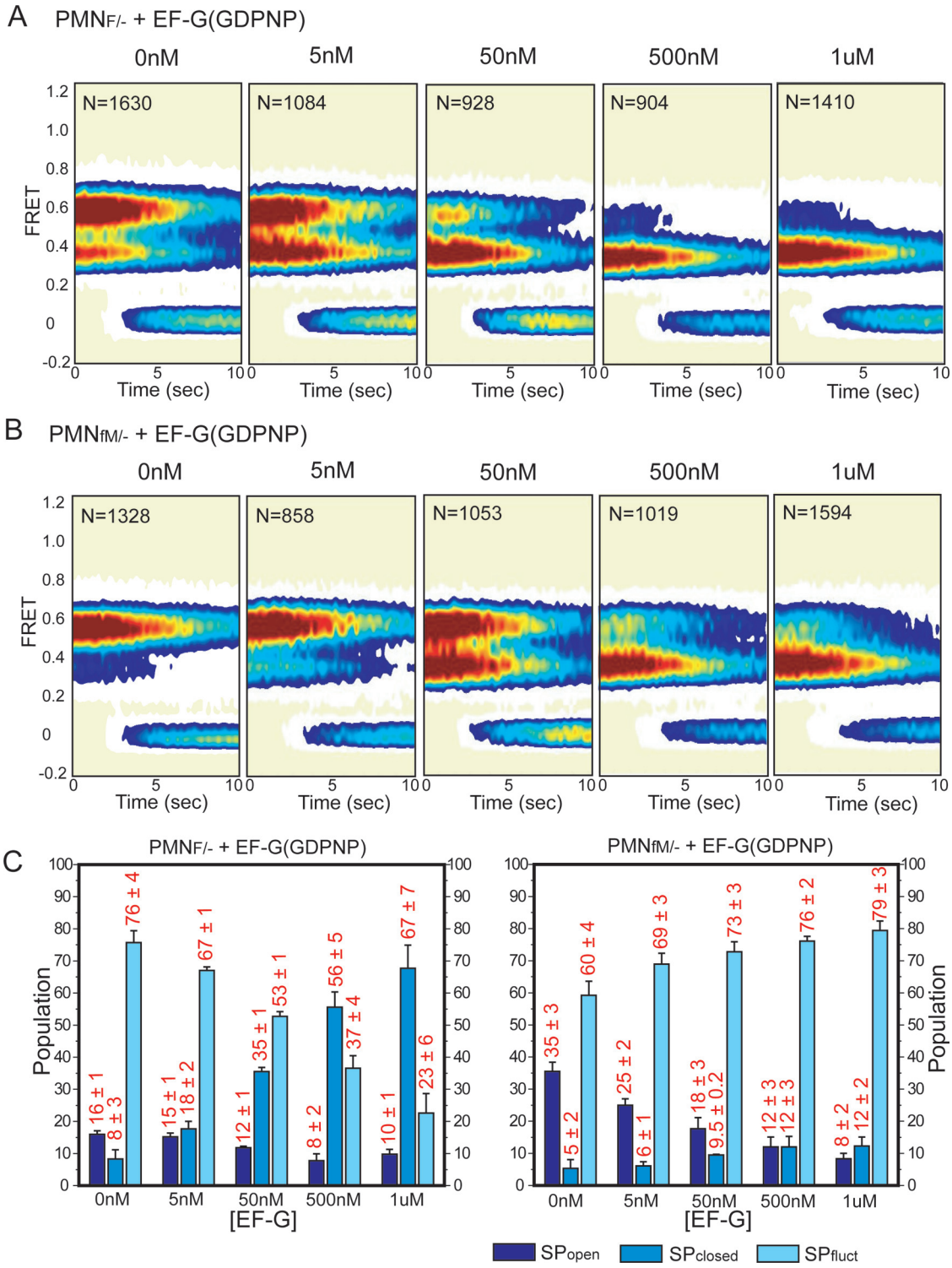

Fig. S4. L1 stalk dynamics as a function of EF-G concentration. (*A*) From left to right, surface contour plots of the time evolution of population FRET for $PMN_{F/-}$ in the presence of 0 nM, 5 nM, 50 nM, 500 nM and 1 μM EF-G; the GDPNP concentration was 1 mM at each EF-G concentration. (*B*) From left to right, surface contour plots of the time evolution of population FRET for $PMN_{fM/-}$ in the presence of 0 nM, 5 nM, 50 nM, 500 nM and 1 μM EF-G; the GDPNP concentration was 1 mM at each EF-G concentration. (*C*) Bar graph reporting the occupancies of SP_{open}, SP_{closed}, and SP_{fluct} as a function of EF-G concentration for $PMN_{F/-}$ (*Left*) and $PMN_{fM/-}$ (*Right*).

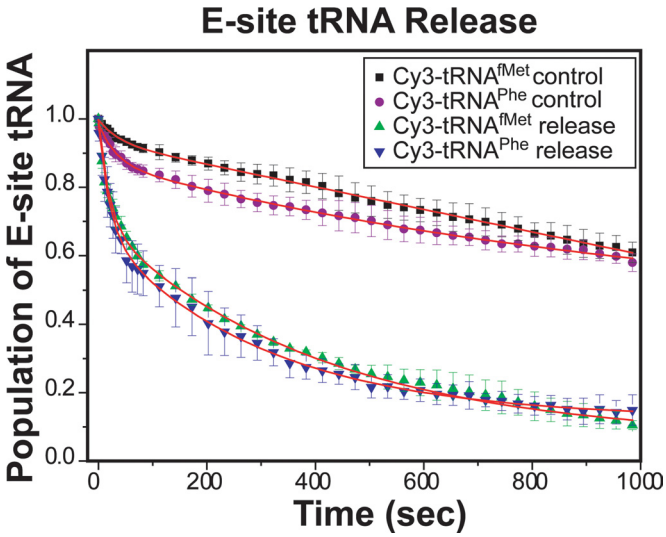

Fig. S5. Single-molecule E-site tRNA release assay. Ribosomal complexes analogous to INI and $POST_{fM/F}$, formed by using 50S subunits harboring a Cy5-labeled L1 and carrying fMet-(Cy3)$tRNA^{fMet}$ or fMetPhe-(Cy3)$tRNA^{Phe}$ at the P site, respectively, were immobilized via a biotinylated mRNA onto the surface of a streptavidin-derivatized quartz flow cell. Spatially localized Cy3 fluorescence from individual surface-immobilized complexes was recorded as a function of time. Stopped-flow delivery of 100 nM EF-Tu(GTP)Phe-$tRNA^{Phe}$ in the presence of 1 μM EF-G(GTP) to initiation complexes resulted in peptide bond formation and translocation of the mRNA-tRNA complex. The translocation event placed the newly deacylated OH-(Cy3)$tRNA^{Phe}$ into the E site. Single OH-(Cy3)$tRNA^{fMet}$ dissociation events from the E site were followed in real-time by monitoring the loss of spatially localized Cy3 signals (green triangles). To reduce the contribution of fluorophore photbleaching to the loss of spatially localized Cy3 signals the 532-nm excitation laser was shuttered at 12 frames min^{-1} for the first 5 frames, 6 frames min^{-1} for the next 5 frames and 2 frames min^{-1} for the last 30 frames. Similarly, release of (Cy3)$tRNA^{Phe}$ is triggered by stopped-flow delivery of 100 nM EF-Tu(GTP)Lys-$tRNA^{Lys}$ in the presence of 1 μM EF-G(GTP) to a POST complex analogous to $POST_{fM/F/-}$ (blue triangles). As a control, the intrinsic loss of spatially localized Cy3 signals due to photobleaching and ribosome dissociation from the surface for both $tRNA^{fMet}$ (black squares) and $tRNA^{Phe}$ (purple circles) were recorded by using identical shuttering parameters. The E-site tRNA release data were best described by double exponential decays (red curves) of the form $A_1*\exp(-t/t_1) + A_2*\exp(-t/t_2) + y_0$ for both $tRNA^{fMet}$ and $tRNA^{Phe}$. The relative populations and lifetimes of the slow and fast dissociating components are reported as the average value taken from three independent measurements. For $tRNA^{fMet}$ (33 $\pm$ 3)% of the population exhibited a lifetime of 20 $\pm$ 6 sec and (67 $\pm$ 3)% of the population exhibited a lifetime of 430 $\pm$ 30 sec, with measurement of the actual dissociation time limited by the photobleaching rate of Cy3. For $tRNA^{Phe}$ (37 $\pm$ 9)% of the population exhibited a lifetime of 20 $\pm$ 3 sec and (63 $\pm$ 9)% of the population exhibited a lifetime of 310 $\pm$ 50 sec.

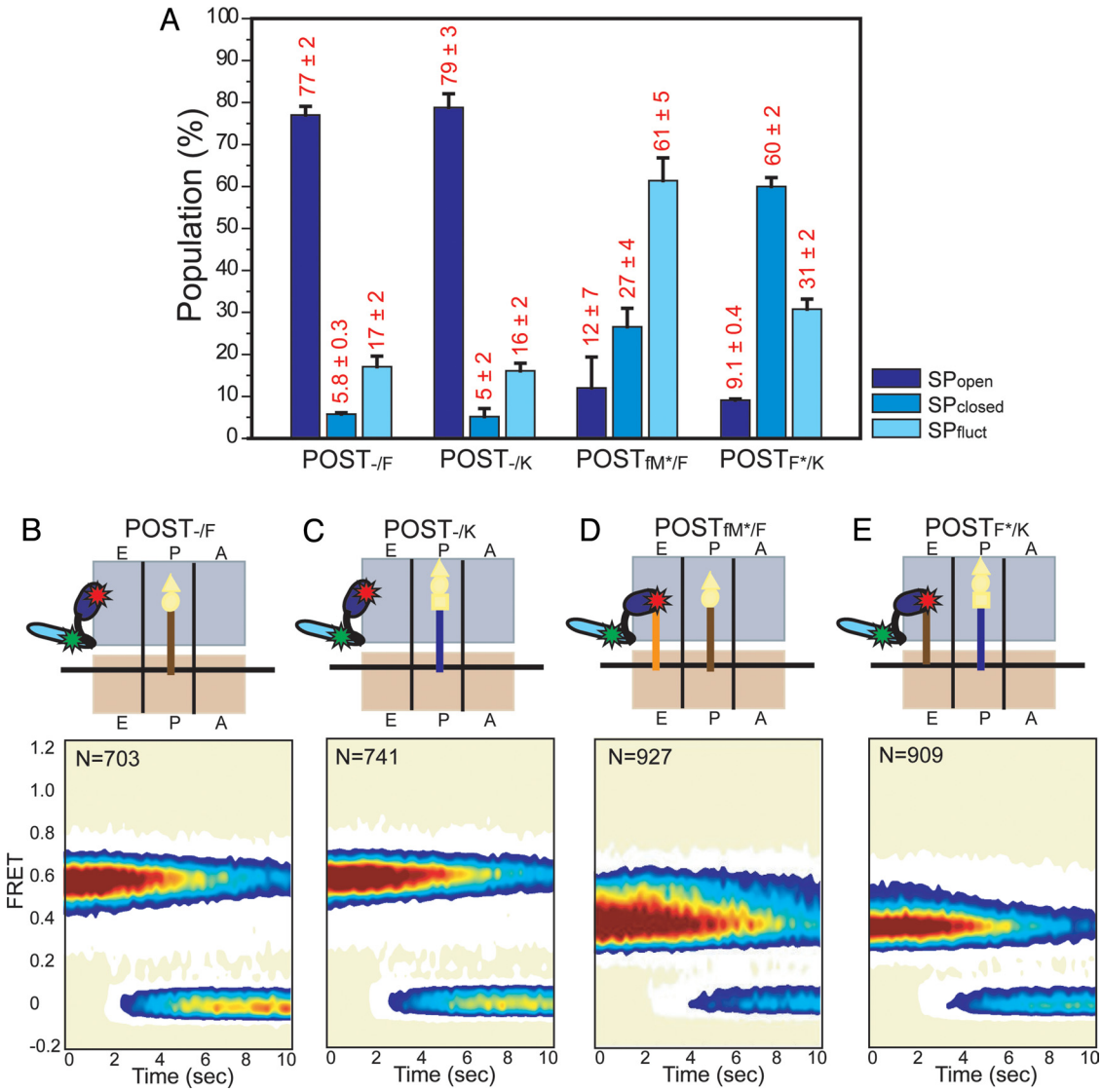

Fig. S6. The effect of the E-site tRNA on L1 stalk dynamics within POST complexes. (*A*) Bar plot of the occupancies of SP_{open}, SP_{closed}, and SP_{fluct} in $POST_{-/F}$, $POST_{-/K}$, $POST_{fM*/F}$ and $POST_{F*/K}$. The means and standard deviations, calculated from three independent datasets, are shown as red numbers. (*B*) Cartoon representation and surface contour plot of the time evolution of population FRET for $POST_{-/F}$, prepared by the addition of 100 nM EF-Tu(GTP)Phe-$tRNA^{Phe}$ and 1 μM EF-G(GTP) to INI in nonpolyamine buffer, followed by incubation at room temperature for 5 min and buffer exchange into Tris-Polymix buffer just before data collection. (*C*) Cartoon representation and surface contour plot of the time evolution of population FRET for $POST_{-/K}$, prepared by the addition of 100 nM EF-Tu(GTP)Lys-$tRNA^{Lys}$ and 1 μM EF-G(GTP) to $POST_{fM/F}$ in nonpolyamine buffer, followed by incubation at room temperature for 5 min and buffer exchange into Tris-Polymix buffer just before data collection. (*D*) Cartoon representation and surface contour plots of the time evolution of population FRET for $POST_{fM*/F}$, prepared by addition of 100 nM EF-Tu(GTP)Phe-$tRNA^{Phe}$ and 1 μM EF-G(GTP) to INI in nonpolyamine buffer, followed by incubation at room temperature for 5 min and buffer exchange into Tris-Polymix buffer, supplemented with 1 μM deacylated $tRNA^{fMet}$, just before data collection. (*E*) Cartoon representation and surface contour plots of the time evolution of population FRET for $POST_{F*/K}$, prepared by addition of 100 nM EF-Tu(GTP)Lys-$tRNA^{Lys}$ and 1 μM EF-G(GTP) to $POST_{fM/F}$ in nonpolyamine buffer, followed by incubation at room temperature for 5 min and buffer exchange into Tris-Polymix buffer, supplemented with 1 μM deacylated $tRNA^{Phe}$, just before data collection.

Table S1. Lifetimes of fluorophores prior to photobleaching from each FRET state

FRET state	Labeled components	Lifetime, sec
0.10*	(Cy5)L1, (Cy3)tRNA^{fMet}	16.3 ± 1.7
0.34†	(Cy5)L1, (Cy3)L9	8.0 ± 1.4
0.56‡	(Cy5)L1, (Cy3)L9	7.7 ± 1.8
0.60§	(Cy5)L1, (Cy3)tRNA^{Phe}	4.0 ± 0.4

Lifetimes are the average values measured from the datasets in which the majority of the sample population stably samples the FRET state designated in the table.

*Lifetime of the 0.10 FRET state is extracted from a ribosomal initiation complex analogous to INI, but carrying the labeled components designated in the table.

†Lifetime of the 0.34 FRET state is extracted from $PMN_{F/-}$ in the presence of 500 nM and 1 μM of EF-G(GDPNP).

‡Lifetime of the 0.56 FRET state is extracted from $POST_{fM/F}$, $POST_{-/F}$ and $POST_{-/K}$.

§Lifetime of the 0.60 FRET state is extracted from a PMN complex analogous to $PMN_{F/-}$ in the presence of 1 μM EF-G(GDPNP), but carrying the labeled components designated in the table.

Table S2. L1 stalk closing and opening rates for $PMN_{F/-}$ and $PMN_{fM/-}$ as a function of EF-G concentration

Complex	[EF-G]*	k_{close} (sec^{-1})				k_{open}, sec^{-1}
		k_1	A_1, %	k_2	A_2, %	
$PMN_{F/-}$[†]	0 nM	0.51 ± 0.06				0.84 ± 0.17
	5 nM	0.62 ± 0.08				0.91 ± 0.03
	50 nM	0.44 ± 0.21	61 ± 9	2.7 ± 0.3	39 ± 9	1.2 ± 0.4
	0.5 μM	0.44 ± 0.23	26 ± 10	3.2 ± 0.3	74 ± 10	1.0 ± 0.2
	1 μM	0.51 ± 0.03[‡]	14 ± 8	2.7 ± 0.7	86 ± 8	1.0 ± 0.2
$PMN_{fM/-}$[§]	0 nM	0.37 ± 0.09				1.5 ± 0.3
	5 nM	0.25 ± 0.09	29 ± 4	2.6 ± 0.7	71 ± 4	1.4 ± 0.1
	50 nM	0.31 ± 0.08	11 ± 9	3.1 ± 0.9	89 ± 9	1.4 ± 0.2
	0.5 μM			2.5 ± 0.6		1.32 ± 0.07
	1 μM			3.0 ± 0.6		1.2 ± 0.2

All rates are derived from dwell time analysis of only those trajectories which occupy SP_{fluct}. Rates reported here are the average and standard deviation from three independent datasets. All rates were corrected for premature truncation due to fluorophore photobleaching as well as the finite nature of the smFRET trajectories (see *Methods* and Table S1).

*The concentration of GDPNP in all experiments was 1 mM.

[†]In this case, trajectories in SP_{fluct} encompass residual amounts of EF-G(GDPNP)-free $PMN_{F/-}$ and EF-G(GDPNP)-bound $PMN_{fM/-}$ and thus the reported rates do not represent EF-G(GDPNP)-bound $PMN_{F/-}$. Instead, A_1 represents the relative population of transition events contributed by EF-G(GDPNP)-free $PMN_{F/-}$ and A_2 represents the relative population of transition events contributed by EF-G(GDPNP)-bound $PMN_{fM/-}$ (*SI Methods*).

[‡]As a consequence of the compositional heterogeneity described in footnote (†), above, and in *SI Methods*, the dwell time histogram for the open L1 stalk conformation was fitted to a double-exponential decay in which the lifetime associated with A_1, τ_1, was set to 1.5 sec [i.e. the lifetime of the open L1 stalk conformation as experimentally measured for $PMN_{F/-}$ in the absence of EF-G(GDPNP)], yielding $k_1 = 0.51\ sec^{-1}$.

[§]A_1 represents the relative population of transition events that are contributed by $PMN_{fM/-}$ that has failed to bind EF-G(GDPNP). A_2 represents the relative population of transition events contributed by EF-G(GDPNP)-bound $PMN_{fM/-}$.